Microscopy and Microanalysis, 2025, **31**, ozaf049
https://doi.org/10.1093/mam/ozaf049
Advance access publication 25 June 2025
Original Article

Microscopy AND Microanalysis

Rapid-Acquisition Fluctuation Electron Microscopy: Decoherence and the Dominant Role of Noise

Armin Zjajo[1], Hongchu Du[2], Rafal E. Dunin-Borkowski[2], J. Murray Gibson[3], Aram Rezikyan[4], and Michael M. J. Treacy[1,*]

[1]*Department of Physics, Arizona State University, Tempe, AZ 85287, USA*
[2]*Ernst Ruska-Centre for Microscopy and Spectroscopy with Electrons, Forschungszentrum Jülich, Jülich 52425, Germany*
[3]*Mechanical Engineering, FAMU-FSU College of Engineering,2525 Pottsdamer Street, Tallahassee, FL 32303, USA*
[4]*Characterization Sciences Department, Corning Inc., 184 Science Center Drive, Painted Post, NY 14870, USA*

*Corresponding author: M. M. J. Treacy, E-mail: treacy@asu.edu

Abstract

We investigate how data acquisition rate affects the decoherence of diffraction speckles in fluctuation electron microscopy (FEM) experiments on amorphous silicon at 80 kV. Surprisingly, reducing acquisition time from 256 ms to 1 ms does not significantly enhance the intensity variance peaks related to medium-range order. This suggests that decoherence processes operate at timescales faster than 1 ms. At the highest acquisition rates, noise complicates the variance background estimation. A significant source of non-Poisson noise is the spread of electron signals across adjacent detector pixels. We mostly restore the discrete pulse counting needed to mitigate Poisson noise by rounding pixel intensity to the nearest integer-electron value. However, a residual negative-variance offset grows as the acquisition rate increases. Efficient electron pulse counting in detectors is crucial for processing Poisson noise in FEM, especially with weak signals.

Key words: amorphous silicon, decoherence, EMPAD detector, FEM, fluctuation electron microscopy, non-Poisson noise, pixel binning, Poisson noise, spatial incoherence

Introduction

Fluctuation electron microscopy (FEM) is a transmission electron microscopy (TEM) method that examines statistical variations in diffraction from small regions of thin amorphous materials to reveal medium-range order (MRO). Unlike crystals, which diffract steady Bragg beams, amorphous materials give a dispersed speckled diffraction that changes between regions. Analyzing speckle intensity variance into scattering vectors $\boldsymbol{k} = (k_x, k_y)$ across multiple regions can reveal MRO, even if the average diffraction pattern appears "diffraction amorphous" (Treacy & Gibson, 1996; Treacy et al., 1998).

The atomic length scale for MRO typically ranges from 1 to 3 nm, while longer-range order manifests as sharper diffraction rings or spots with crystallographic *hkl* indices (Treacy et al., 2005). The speckle variance from MRO is strongest when the sampled-volume width, controlled by microscope resolution, is comparable to the characteristic MRO length scale (Treacy & Gibson, 2012). Being a low-resolution technique, FEM is not significantly affected by depth-of-focus issues for typical sample thicknesses. Since FEM examines diffraction intensity as a function of probed location, $I(x, y; k_x, k_y)$, it is an early example of 4D Microscopy (Nellist et al., 1995; Ophus, 2019).

FEM is not a quantitative technique like Rietveld refinement or pair-distribution function (PDF) analysis in X-ray diffraction. A key challenge is that experimental variance measurements are much weaker than kinematical scattering predictions. Theory and simulations with coherent illumination indicate that the intensity histogram of scattering into vector $\boldsymbol{k}$ from a disordered sample follows a negative exponential probability distribution:

$$P(I) = \frac{1}{\langle I \rangle} \exp\left(-\frac{I}{\langle I \rangle}\right). \quad (1)$$

$\langle I \rangle$ is the mean intensity, and the normalized variance, obtained by dividing the variance by $\langle I \rangle^2$, equals 1.0. When MRO is introduced into models, broad normalized variance peaks emerge above this background as a function of $\boldsymbol{k}$ (Treacy & Gibson, 1998; Rezikyan et al., 2015). However, experimental FEM data typically yield background-normalized variance values of 0.001 to 0.05, a significant discrepancy. Deceptively, experimental diffraction data from thin amorphous materials seem to be well modeled by kinematical scattering: quantitative pair-distribution details can be extracted, elucidating the short-range order (SRO) (Cockayne & McKenzie, 1988; Cockayne, 2007). PDF measurements are relatively insensitive to decoherence effects because large volumes are probed and the absolute position in space relative to the incident beam position (phase) is unimportant as long as no rotations occur during exposure. For amorphous materials, rotations can be quite large without much effect on the short-range interference. Even small wavelength shifts are unimportant. Additionally, the beam fluences are many orders of magnitude smaller because of macroscopic averaging in diffraction. In FEM, small volumes are examined and the absolute position relative to the probe becomes more important, thus small displacements can have a significant effect.

Received: March 2, 2024. **Revised:** May 14, 2025. **Accepted:** May 20, 2025

Combinatorially, there are many more degrees of freedom affecting the 4-body (pair–pair) interactions that dominate the FEM signal than there are for the 2-body (pair) interactions in the PDF. Consequently, FEM exhibits enhanced sensitivity to incoherence and decoherence effects (Treacy & Gibson, 1998).

Monte Carlo methods, which match mean diffraction and normalized variance data by adjusting model atom locations, have had success when a multiplicative parameter is introduced to emulate the variance suppression phenomenologically (Borisenko et al., 2012; Kalay et al., 2012; Treacy & Borisenko, 2012; Maldonis et al., 2017). Despite the difficulties matching experimental variance peak *amplitudes*, the peak *locations* tend to match those in simulations from well-characterized models.

As outlined above, illumination spatial incoherence reduces speckle variance, especially in the background. Each incident electron has an extensive oscillatory coherence volume whose phase gradients are not necessarily aligned with those of other incident electrons. The relative scattering phase, $2\pi\Delta\boldsymbol{k}\cdot\boldsymbol{r}_{ij}$, when atoms i and j are far apart, can vary significantly with small changes, $\Delta\boldsymbol{k}$, in the incident wavevector. The time-averaged coherence volume, within which the relative scattering phase does not vary by more than about $\pi/2$, contracts to the immediate neighborhood, $\{\boldsymbol{r}_{ij}\}$, of each atom i, elongated along the beam direction (Gibson & Howie, 1979; Treacy & Gibson, 1996; Treacy et al., 2005).

In early FEM experiments, spatial coherence was treated as an adjustable parameter. Hollow-cone dark-field imaging (HCFEM) in a TEM analyzed image speckle intensity variance as a function of the hollow-cone tilt vector, which controls the coherence volume (Treacy & Gibson, 1996). Background variance from uncorrelated atoms was strongly suppressed, highlighting local MRO contributions, and this initially masked the numerical discrepancy between theory and experiment for coherent illumination.

Later, the intensity histogram of amorphous carbon was analyzed using tilted dark-field FEM in a TEM (TDFEM) (Treacy, 2012; Rezikyan et al., 2015). Intensity histograms fit a Gamma distribution (Treacy, 2012; Rezikyan et al., 2015), as predicted for partially coherent illumination (Dainty, 1975; Goodman, 1975*a*, 1975*b*), represented by:

$$P(I)=\frac{m^m}{\Gamma(m)}\frac{I^{m-1}}{\langle I\rangle^m}\exp\left(-\frac{mI}{\langle I\rangle}\right). \tag{2}$$

The parameter $m\geq 1$ governs the distribution's profile, which can be derived as an $(m-1)$-fold convolution of negative exponentials, with $\Gamma(m)=(m-1)!$ for integer m. It was suggested that m measures the number of incoherent sources in the illumination (Treacy & Gibson, 1998). The Gamma distribution has a normalized variance of $1/m$, with $m=1$ corresponding to full spatial coherence. Surprisingly, high values of $m\approx 35$ were found, seemingly inconsistent with the high coherence suggested by the bright-field Fresnel fringes.

In scanning transmission electron microscope (STFEM) experiments, illumination coherence was estimated by comparing focused-probe images with the Airy disk. Zjajo et al. (2021) found a range $1.5\leq m\leq 23$, with higher m values linked to larger condenser spot sizes, which provide higher beam current and lower shot noise but much-reduced coherence.

The origins of background variance suppression have been explored using STFEM (Rezikyan et al., 2015; Radić et al., 2019, 2022). Rezikyan et al. (2015) proposed that signal decoherence occurs during scattering and data collection, possibly from rapidly fluctuating phase shifts in scattered electron waves. Fluctuations in phase $2\pi\boldsymbol{k}\cdot\boldsymbol{r}_{ij}$ can arise from rapid changes to the irradiated atom positions $\Delta\{\boldsymbol{r}_{ij}\}$ (displacement decoherence) in addition to the variations $\Delta\boldsymbol{k}$ in the incoming beam (illumination spatial incoherence). Significant atomic movement during acquisition averages fine-scale details, reducing variance. Simulations indicate that phonons are not a significant issue and suggest that random atomic vibrations with a root-mean-square amplitude of 1.5 Å reproduce key experimental features. However, such large displacements are questionable in lightly beam-damaged samples. More likely mechanisms include bulk motions like specimen drift, film vibrations, phase changes, and material rotations. Other contributors may include sample charging variations, aperture charging modes (objective apertures are smaller in FEM), inelastic scattering, and multiple scattering.

Decoherence mimics spatial incoherence by conforming to Gamma-distribution intensity statistics (Rezikyan et al., 2015). This suggests an *adherence volume* around each scatterer, similar to the coherence volume, wherein scattering remains sufficiently mutually coherent throughout the diffraction pattern acquisition time. We expect the adherence volume to shrink with increasing acquisition time if the sample changes continuously under the beam.

Lower beam fluence in the probed volume can reduce specimen damage and fluctuations from sample charging from secondary electron emission (Jiang, 2015, 2016, 2023). Rezikyan et al. (2015) suggested faster diffraction acquisition times may lessen decoherence effects, particularly from slower motions like drift. However, reduced fluence increases variance from Poisson shot noise, which competes with the structural variance being studied.

High frame-rate direct electron detection cameras, with high detective quantum efficiencies (DQE near 1.0) and excellent modulation transfer function (MTF) characteristics, enable the exploration of decoherence in FEM at faster sample perturbation frequencies.

This report examines how fast exposure times, down to 1 ms with an 80 kV beam on an electron microscope pixel array detector (EMPAD), affect the normalized variance of amorphous silicon thin films. An unexpected complication of this study was non-Poisson noise on the EMPAD.

Experimental Details

Data were collected on the FEI Titan G2 80–200 ChemiSTEM, a probe-corrected analytic scanning transmission electron microscope (STEM). The X-FEG source brightness was 7.5×10^7 A m^{-2} sr^{-1} V. The beam voltage was 80 kV, below the knock-on damage threshold for *crystalline* silicon. The probe size (resolution) was ~ 1.1 nm using gun lens setting 8, objective aperture diameter 50 μm, and spot size 11.

The instrument features an EMPAD with a 128×128 pixel array, each pixel measuring $150\,\mu\text{m}\times150\,\mu\text{m}$ and $500\,\mu$m thickness (Tate et al., 2016). It has a dynamic range of 30 bits and registers 151 analog-to-digital units (ADU) per incident electron at low fluence, with a baseline noise of 2.8 ADU. The maximum frame rate is 1.1 kHz with a readout time per frame of 0.86 ms. The shortest acquisition time we used was 1 ms. The detective quantum efficiency (DQE) is

0.88 at approximately 0.2 electrons/pixel/frame and is estimated to reach 0.93 at around 700 electrons/pixel/frame at 80 kV.

There was no Faraday cup to measure current. The fluence rate was evaluated to be $1.06 \pm 0.21 \times 10^7$ electrons/nm^2/s, about 1.1 pA, using the EMPAD diffraction patterns corrected for estimated scattering beyond the collection solid angle.

The diffraction camera length was 0.28 m, confirmed by diffraction from gold particles on a thin carbon film. With the unscattered beam centered at pixel (64,64), the scattering range is $-8.1 \lesssim k_x, k_y \lesssim 8.1\,\text{nm}^{-1}$, each pixel subtending Δk of $0.126\,\text{nm}^{-1}$/pixel.

In a previous report (Zjajo et al., 2021), the illumination spatial coherence was estimated by comparing the probe intensity profile to an ideal Airy disk, yielding $m \sim 1.5$. Ideally, the normalized variance baseline value is expected to be $1/m \approx 2/3$ for a random structure.

We examined three amorphous silicon specimens with thicknesses of 5, 9, and 15 nm from SPI, Inc. (catalog numbers US100-A05Q33A, US100-A09Q33, US100-A15Q33, lot# 1270927). They were produced via a proprietary sputtering process on crystalline silicon wafers, which were then etched to create freestanding membranes. The films have a uniform thickness (less than 0.3 nm r.m.s. surface roughness) and a thin oxide layer on both surfaces. Details about gases and pressures are proprietary. Diffraction and FEM data suggest the oxide layer is the minority phase, even in the 5-nm samples.

Five experiments were conducted with 256, 64, 16, 4, and 1 ms frame acquisition times for each film thickness. To keep a constant total signal, the acquisition times, τ, and the number of diffraction patterns, N, were adjusted to satisfy

$$N \times \tau = 65{,}536 \quad \text{patterns.ms.} \tag{3}$$

Accordingly, patterns were acquired from square scan arrays ranging from $N = 16 \times 16$ to 256×256 patterns—the sampling size increasing as acquisition time decreases. Freshly scanned areas were 2.6–2.9 μm across, ensuring that probed regions were more than 10 nm apart. For the 5-nm thick amorphous Si films, approximately 4.5×10^8 electrons were collected in each experiment. A 1-ms exposure yielded about 6,900 electron counts per pattern, 85% of which fall inside $k \lesssim 1\,\text{nm}^{-1}$, in and around the central beam.

Modeling and Analysis

Data processing and modeling were conducted using our C codes. The intensity was tracked by defining a region of interest (ROI) in diffraction patterns with ImageJ (Schneider et al., 2012). Annular ROIs, centered on the diffraction origin, monitored intensity in diffraction rings. The total intensity and Pearson r factor (Press et al., 1992) for pixels within the ROI were analyzed across frames to assess linear correlations between successive diffraction patterns from the same sample region. When correlated, $r = \pm 1$. Loss of correlation ($r \to 0$) indicates decoherence between successive diffraction patterns.

When rastering the probe, diffraction patterns were sometimes shifted by up to three EMPAD pixels, presumably because of tilt-purity misalignments. Conceivably, charge build-up on the sample during the scan might be deflecting the incident beam. Our code compensated by shifting patterns back to the origin to the nearest half-pixel.

The variation in intensity at scattering vector (k_x, k_y) is measured by the normalized variance, defined as:

$$\text{nVar}(k_x, k_y) = \left(\frac{N}{N-1}\right)\left[\frac{\langle I^2(k_x, k_y)\rangle_N}{\langle I(k_x, k_y)\rangle_N^2} - 1\right]. \tag{4}$$

$\langle\ \rangle_N$ represents the average over all probe positions (x_n, y_n) for $n = 1$ to N. $\langle I(k_x, k_y)\rangle_N$ is the mean intensity, while $\langle I^2(k_x, k_y)\rangle_N$ is the mean of the squared intensity. The prefactor $N/(N-1)$ arises because, strictly, the variance computation has only $N-1$ independent degrees of freedom—there is no variance when $N = 1$. When N is large, this scaling factor tends to 1.0 and is usually ignored. However, it may be important to include it when correcting for noise, as discussed later. Normalization by $\langle I(k_x, k_y)\rangle_N^2$ compensates for the decrease in electron scattering factor as $k = \sqrt{k_x^2 + k_y^2}$ increases. We refer to this as "nVar," "nVarNC" (noise corrected), or simply "the variance" when the context is clear. nVar(k_x, k_y) provides a 2D normalized variance map. In simulations, a disordered sample shows a uniform variance across scattering vectors, and MRO introduces additional peaks or rings.

Diffraction simulations were based on kinematical scattering from stationary atoms using a 4,096-atom silicon continuous random network (CRN) with a cubic unit cell edge of 4.524 nm (Wooten et al., 1985). A single cell was randomly oriented over 4π steradians, and the probe was randomly displaced laterally to avoid oversampling of the model's center. Diffraction for each orientation was calculated on a $1{,}024 \times 1{,}024$ grid out to $\pm 13\,\text{nm}^{-1}$, centered at (512, 512). The probe was modeled using a Gaussian intensity profile with a standard deviation of 0.378 nm, equivalent to a resolution of 1 nm per the Rayleigh resolution criterion, where the intensity dip between resolved points is $8/\pi^2$ of the peak intensity (Born & Wolf, 2013). Diffraction-limited Airy-disk profiles yielded similar results but were computationally slower.

We generate radially averaged plots by a method similar, but not formally identical, to Daulton's method 4, the "annular mean of variance image" (Daulton et al., 2010). P copies of each of the N diffraction patterns are made and rotated about the origin by an angle $2\pi(p-1)/P$, $p = 1, \ldots P$. Bilinear interpolation was used to determine pixel intensities in the rotated patterns. For the EMPAD, $P = 400$ is sufficient. Each rotated copy is treated as a valid distinct diffraction pattern, and the variance map of the enlarged ensemble of $N \times P$ patterns is computed. P was adjusted so the resultant variance map has azimuthally smooth rings. The trace nVar$(k, 0)$ is taken to represent the azimuthally averaged variance, nVar(k). Aliasing near the origin, with the fewest pixels per annular ring, introduces small spurious variance features. Variance around the origin is low and not usually of structural interest. Our nVar(k) plots are restricted to the inscribed circle of the square pixel array centered at the diffraction origin, and data in pattern corners are ignored.

When the signal is weak, shot and detector noise dominate variance. Shot noise follows a Poisson distribution and was apportioned randomly as discrete counts using the method of Gibson & Treacy (2008). The probability of a discrete measure q (for example, the number of electrons collected in a pixel over some time interval) with mean $\langle q\rangle$ is:

$$P(q, \langle q\rangle) = \frac{\langle q\rangle^q}{q!}\mathrm{e}^{-\langle q\rangle}. \tag{5}$$

The variance equals $\langle q \rangle$. Thus, the normalized variance is $1/\langle q \rangle$. For a perfect detector, the normalized variance can be corrected for the Poisson-noise background:

$$\mathrm{nVarNC}(k_x, k_y) = \left(\frac{N}{N-1}\right)\left[\frac{\langle I^2(k_x, k_y)\rangle_N}{\langle I(k_x, k_y)\rangle_N^2} - 1\right] - \frac{1}{\langle I(k_x, k_y)\rangle_N}. \quad (6)$$

Intensity must be recorded as discrete electron counts. $N/(N-1)$ The EMPAD does not count pulses, and scaling intensity by $I_e = 151$ ADU units/electron (at 80 kV) leads to fractional counts, and the noise correction fails for weak signals ($I \lesssim 10$). Using the nearest-integer value $I = \mathrm{nint}(I_{\mathrm{ADU}}/I_e)$ stabilizes the noise correction, allowing interpretation of variance peak heights relative to the background.

Understanding electron detectors' noise and response characteristics is crucial for quantitative electron microscopy (Ruskin et al., 2013; Lee et al., 2014; Tate et al., 2016; Levin, 2021; Kodama et al., 2022). Equation (6) has no adjustment for the detective quantum efficiency (DQE < 1) as noise cannot be further randomized. It corrects the formula from Treacy et al. (2005), who proposed a noise correction term $-\mathrm{DQE}/\langle I(k_x, k_y)\rangle_N$, which works deceptively well for nondiscretized experimental data with moderate noise levels. This issue of noise discretization is important and is examined in the Results and Discussion.

Results

EMPAD Noise Characteristics

Figure 1 plots the time evolution of diffraction intensity from a 5-nm thick amorphous silicon sample into two 8×8 pixel regions of reciprocal space—indicated by the inset red and blue squares. We collected 25,000 patterns over 46.5 s, allowing for the 0.86 ms readout time. The electron flux into each region is presented as I_{ADU}/I_e electron counts. In addition to high-frequency shot noise, both regions show intensity variations at timescales of 1–3 s, potentially from specimen drift, tilts, structural rearrangements, or sample charging. The average counts scattered from the central beam remain essentially constant, indicating no significant loss of Si or carbon contamination buildup.

Figure 2a shows the I_{ADU}/I_e electron counts from the green 8×8-pixel ROI in Figure 1, centered around $k \approx 2\ \mathrm{nm}^{-1}$, selected for its weak structural speckle. The intensity histogram in Figure 2b (green circles) is fitted to a Gaussian (blue curve). For a Poisson distribution to approximate a Gaussian, the mean should be $\langle q \rangle \gtrsim 10$. The mean is 17.3 electron counts with a standard deviation of 4.7. A Poisson distribution with this mean has a standard deviation of $\sqrt{17.3} \approx 4.2$ (red curve). The good agreement indicates that most intensity variation in the green ROI is from Poisson noise, with a contribution from longer timescale variations.

Figure 3 shows the low-intensity end of the diffraction-pattern intensity histograms, recorded from 27,000 1-ms diffraction patterns from the 5-nm thick amorphous Si sample. The last 2,000 frames have the incident beam blanked. The horizontal bands indicate statistical detection of 0- to 4-electron arrival events, with the right plot displaying the accumulated histogram of the first 25,000 patterns. The peak at zero electron counts is pronounced. The 1-electron peak is less sharp, and higher-count peaks are increasingly broadened with no discernible peak for five electrons. Notably, there is significant intensity for nondiscrete electron counts, and the rate for a "1/2 an electron" event is about half that for "1 electron." The horizontal red lines indicate the ideal detector's response.

The broadened histogram peaks can be partly explained by examining individual pixels in 1-ms diffraction patterns away from the central beam. Figure 4 shows six enlarged EMPAD pixel patches from a diffraction pattern near $k \sim 6.5 \pm 0.5\ \mathrm{nm}^{-1}$

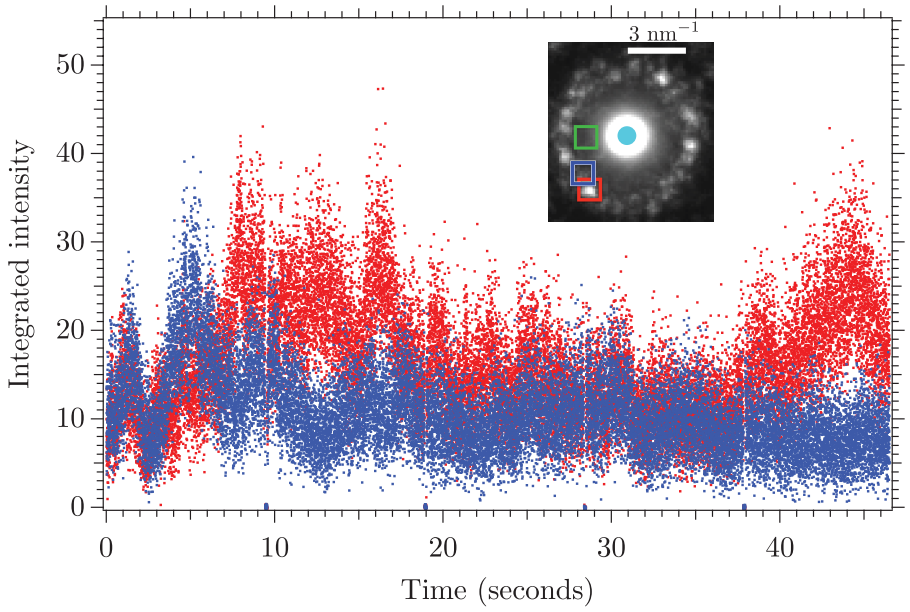

Fig. 1. Plots of diffracted intensity as a function of time accumulated into two 8×8-pixel diffraction windows. Data are from 25,000 1-ms-exposure diffraction patterns acquired from a fixed location in a 5-nm thick amorphous Si sample. The red and blue plots are from the red and blue regions of interest indicated in the inset averaged pattern. The unscattered central disk is outlined in light blue. Results from the green region are presented in Figure 2.

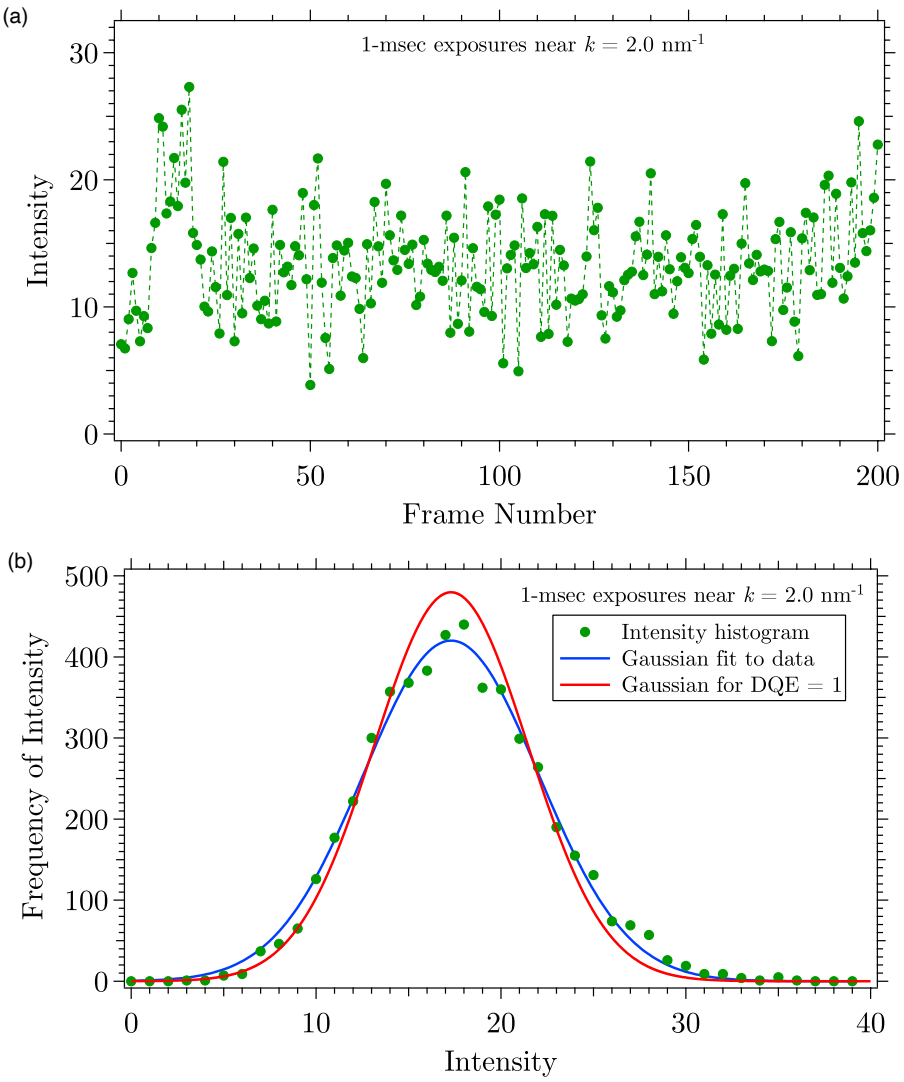

Fig. 2. (**a**) Plot of the total intensity accumulated in the green 8 × 8-pixel window shown in Figure 1. The data from the first 200 1-ms frames are displayed. The dashed lines connect successive data points. (**b**) The intensity histogram (green points) from the full set of 25,000 patterns. The histogram is fitted to a Gaussian (blue curve). The narrower red curve is the Gaussian expected at this mean intensity for a perfect detector.

where scattering is weak. Ideally, detected electrons appear as single bright pixels such as Figure 4a with a signal of $I_{\mathrm{ADU}} = 153$ ADU for 1.01 electrons. Figure 4b illustrates a single electron event spread across two pixels summing to 0.96 electron units, while Figure 4c represents an event spread over three pixels totaling 1.2 electrons. Most single-electron events fit these scenarios, contributing to the noninteger spread in Figure 3.

Quantizing pixel intensity to the nearest integer value, $\mathtt{nint}(I/I_e)$, is effective for single-electron events, such as those in Figures 4a–4c. However, it can misidentify the incident pixel. Examples of failure are shown in Figures 4d–4f. In Figure 4d, a total signal of 1.96 suggests two electrons, but `nint` registers only one at pixel 0.70. Figure 4e shows a single-electron event spread over four pixels, yet `nint` reports zero. Figure 4f indicates a likely 2-electron event, but only one is recorded at pixel 1.36.

The `nint` threshold does not conserve the total signal; at 80 kV, it results in a signal loss of −4.4% compared to the raw sum. We explored noise corrections of the form $-Q/\langle I\rangle$, aiming for $Q \approx 0.956$, but deviations from $Q = 1$ led to unstable corrections at higher k.

Electron Correlation Microscopy

The longer timescale intensity fluctuations in Figures 1 and 2 were investigated using electron correlation microscopy (ECM). Figure 5 presents results from 4-ms diffraction patterns from a 9-nm thick amorphous Si sample, averaging five experimental runs from different areas. Because of shot noise, the Pearson r factor starts at 0.29 and decays to 0.18. The 1-ms diffraction data on the 5-nm sample was too noisy to analyze, with $r \approx 0.04$.

Several mechanisms can cause correlation loss between diffraction patterns: specimen drift, accumulated beam damage, thermodynamical changes, contamination, and changes in charge distributions. Vaerst et al. (2023) studied the role of beam effects on long-timescale atom dynamics in metallic glasses, where drift is a concern. Our broad annular ROI over diffraction k-space averages over a range of dynamics (Huang & Voyles, 2024). Nevertheless, we fitted the correlation decay to a single exponential-decay function, $r = r_0 + A\exp(-t/T)$, finding $r_0 = 0.184$, $A = 0.113$, and time constant $T = 272$ ms, slightly longer than our longest acquisition time of 256 ms. r_0 indicates the residual correlation

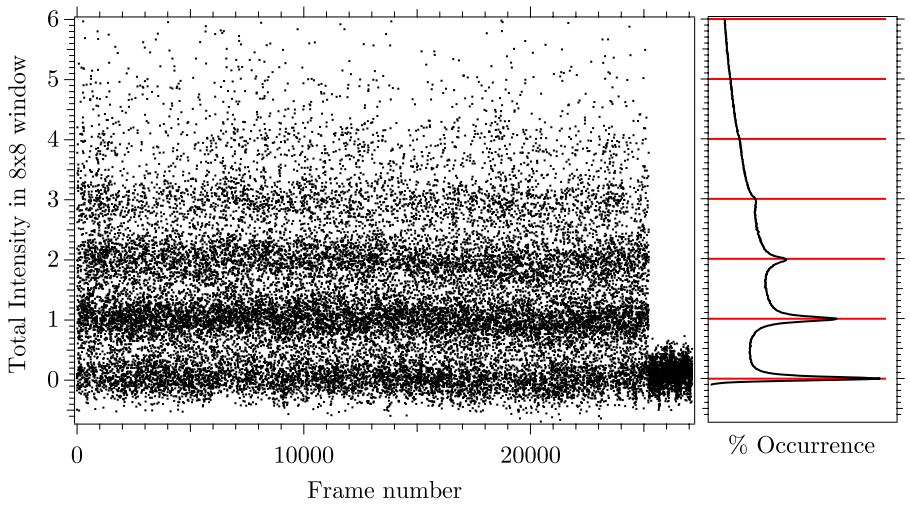

Fig. 3. Left: The low-intensity end of the intensity histograms of the 1-ms diffraction data from 5-nm thickness amorphous Si, displayed along the vertical axis as electron counts, as a function of the frame number (horizontal axis). The time scale is the same as for Figure 1. Horizontal bands appear at 0, 1, 2, 3, and 4 electron counts. The 2,000 points at the end of the run are for the blanked beam. Right: the averaged intensity histogram for the first 25,000 patterns. The horizontal red lines indicate the idealized delta-function response of the perfect detector.

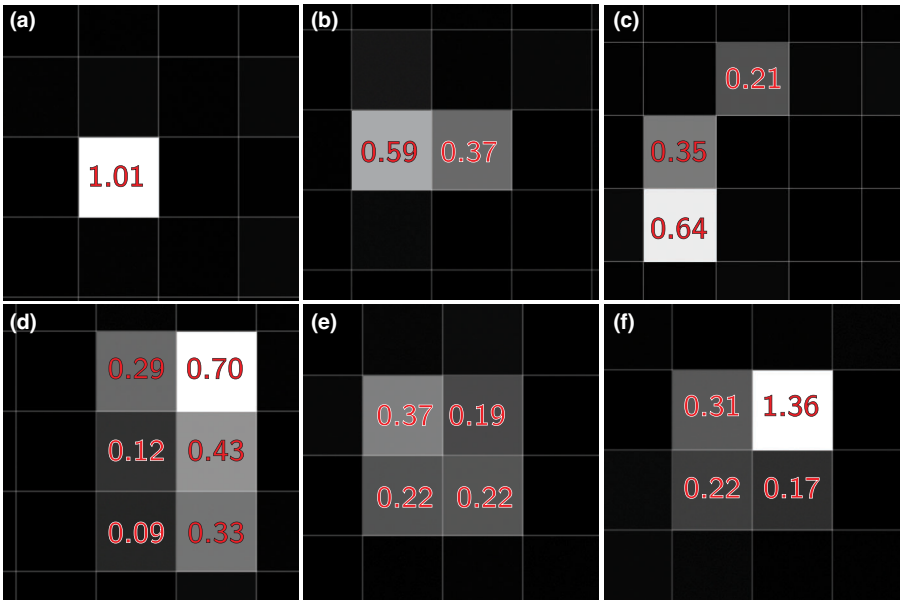

Fig. 4. Examples of single- and double-electron capture events on the EMPAD. The nominal, nondiscrete number of electrons collected by each pixel is indicated. (**a**) A single-electron event, confined mostly to one pixel. (**b**) A single-electron event spread over two pixels. The nearest-integer threshold, `nint`, will register one electron for 0.59. (**c**) A one-electron event. `nint` registers 1 electron at 0.64. (**d**) Two electron events, but `nint` registers only one electron at 0.70. (**e**) The total signal is 1.0, a likely single electron event, but `nint` registers zero. (**f**) There are two electron events, but `nint` registers only one electron at 1.36.

among unrelated diffraction patterns with the same electron scattering factor profile.

Fluctuation Electron Microscopy

Figure 6 summarizes experimental FEM data for the 5-nm amorphous Si film across five exposure times: $\tau = 256$, 64, 16, 4, and 1 ms, with similar data for 9-nm and 15-nm samples. Recall that the number of diffraction patterns N was set to ensure $N\tau = 65{,}536$, maintaining a consistent total signal for each dataset.

The left column shows individual diffraction patterns. In the 256-ms data (top left), diffraction speckles from the amorphous Si structure are visible, with speckle width corresponding to the diameter of the central diffraction disk, about $1.22/(1.1\,\text{nm}) = 1.1\,\text{nm}^{-1}$ (nine pixels). In the 1-ms pattern (bottom left), the structural speckles are indiscernible to the eye against the noise.

The mean diffraction patterns in the second column are essentially identical. The normalized variance maps, $\text{nVar}(k_x, k_y)$ in the third column, show significant noise variance at higher k values in the edges and corners. The two characteristic variance rings of amorphous Si are visible in the 256-ms data, while the maps for $\tau \leq 64$ ms show a single bright ring where we expect a dip between those two rings. This contrast reversal is because

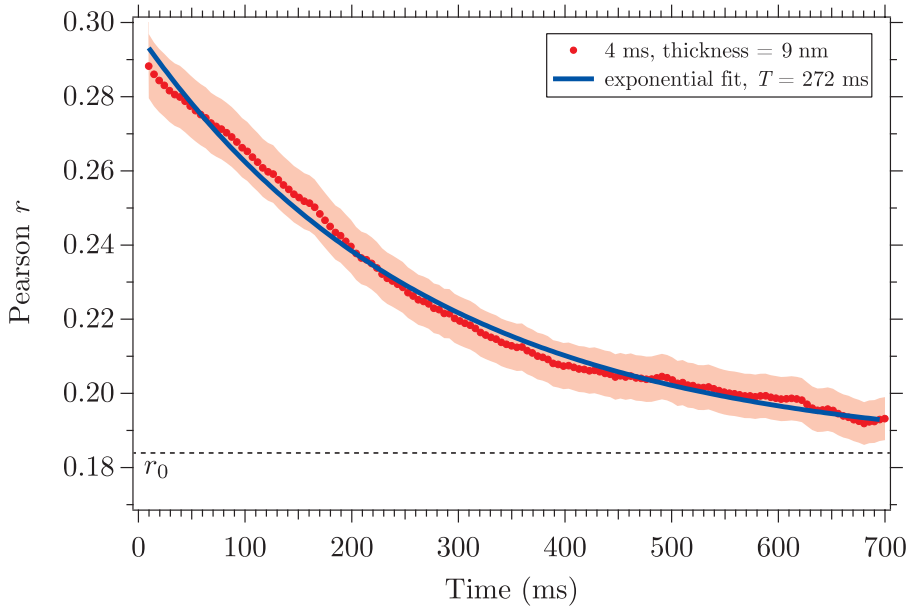

Fig. 5. Pearson r correlation analysis of the 4-ms data from 9-nm thickness amorphous Si (red points), averaged over five separate runs. The shading represents the spread of those runs. The Pearson r immediately drops from 1.0 to $r \approx 0.29$ because of strong Poisson noise. The blue line is a fit to an offset negative exponential, indicating a decay-time coefficient $T = 272$ ms. The noise baseline at large times is $r_0 = 0.184$.

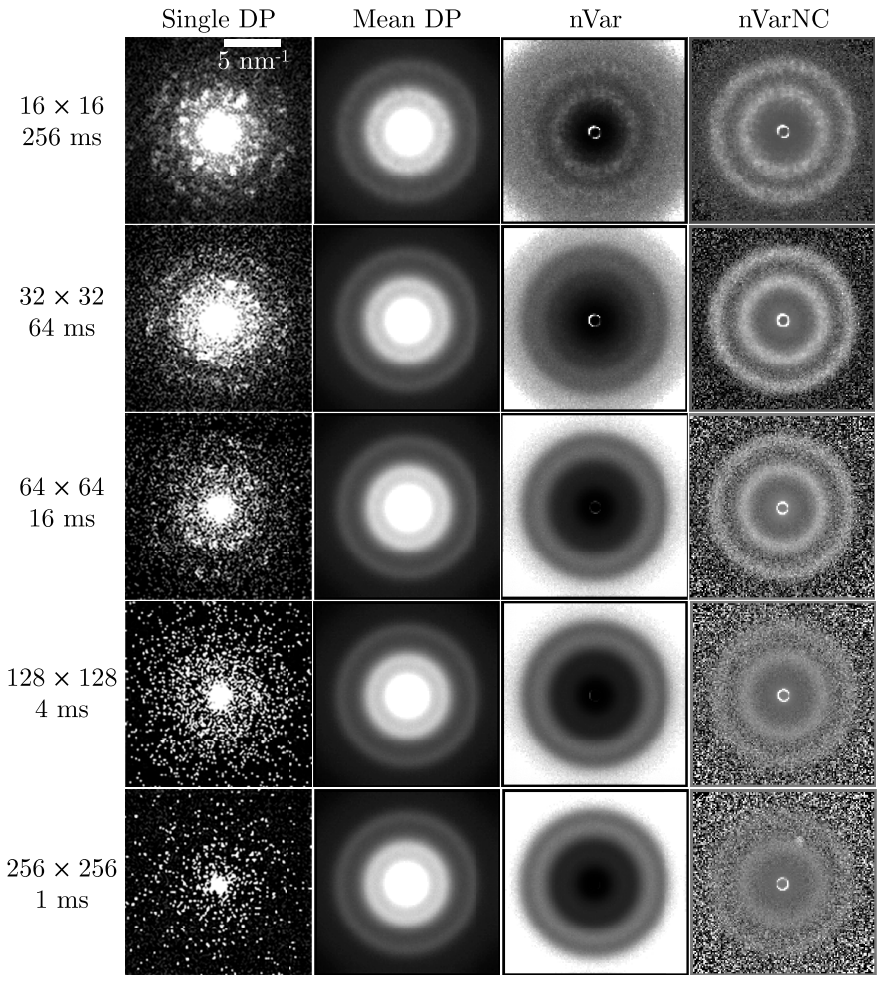

Fig. 6. Summary of experimental diffraction data acquired for 5-nm thickness amorphous Si. Data for the five exposure times are presented in the rows, top to bottom, $\tau = 256$, 64, 16, 4, and 1 ms. The left column presents a typical diffraction pattern from each series. The second column presents the mean diffraction patterns. The third column presents the normalized variance maps. The fourth column displays the noise-corrected normalized variance maps using `nint` thresholding. Values in the range $0 \leq \text{nVarNC} \leq 0.3$ are displayed.

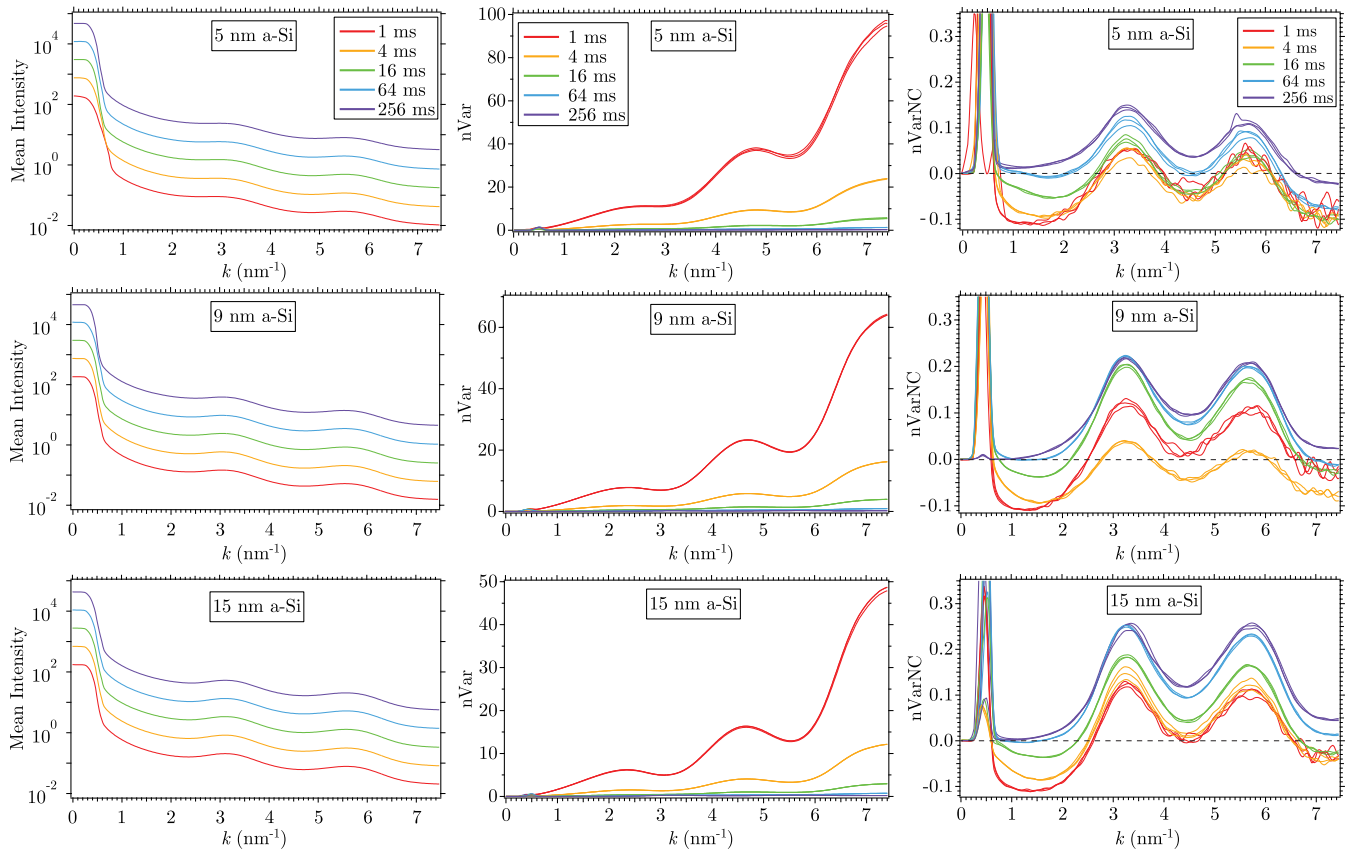

Fig. 7. Montage showing the radial intensity and variance data for three thicknesses of amorphous silicon. Before processing, all data have been discretized, nint(I/I_e). The rows present data for silicon thicknesses of 5 nm (top), 9 nm (middle), and 15 nm (bottom). The columns show: left, the mean diffraction patterns on a logarithmic scale; middle, the normalized variances, nVar; right, the Poisson-noise corrected normalized variances, nVarNC. Three plots are presented for each experiment to indicate experimental variation.

of Poisson noise variance, which is large where $\langle I(k_x, k_y)\rangle_N$ is weak (i.e. in the dip). The `nint`-thresholded variance maps, nVarNC(k_x, k_y) in the fourth column, remove much of the shot-noise variance and restore the two characteristic a-Si variance rings at $k \approx 3.2$ and $5.7\,\mathrm{nm}^{-1}$. A sharp variance feature at the rim of the central disk near $k \approx 0.55\,\mathrm{nm}^{-1}$ arises from the half-pixel precision in the pattern-shift correction of the tilt-purity misalignment.

The nVarNC maps present a visual intensity scale ranging from 0 (black) to 0.3 and above (white). A slight negative offset increases as exposure time decreases, causing parts of the variance map to "submerge" at shorter exposures, with the tops of the two rings visible as "islands." The amplitude of the nVarNC rings, compared to the dip between them, is consistent across all five experiments.

Figure 7 presents radial plots of results for the three amorphous Si thicknesses. Data from three experimental runs for each thickness and exposure time are shown, with overlapping plots indicating reproducibility. The data were processed as `nint`(I/I_e). The top row represents 5-nm a-Si, the middle for 9-nm a-Si, and the bottom for 15-nm a-Si. Mean diffraction profiles, $\langle I(k)\rangle$, are in the left column on a logarithmic scale. Notwithstanding the fourfold increments in exposure times, the mean diffraction profiles for each thickness are identical. Two diffraction peaks near 3.2 and $5.7\,\mathrm{nm}^{-1}$ appear in all mean plots but are less distinct in the 5-nm data, possibly because of the thin oxide layers: the 5-nm film would have the lowest silicon/silica ratio if the oxide thickness is consistent.

The center column shows the `nint`-thresholded variances, nVar. nVar increases rapidly with increasing k where noise dominates the variance. nVar is highest for the thinnest samples, reaching nVar ≈ 100 for $k \geq 7.5\,\mathrm{nm}^{-1}$, where the signal-to-noise ratio is lowest.

The third column displays the Poisson-corrected variance (nVarNC, `nint`-thresholded). The negative offset is observed across all thicknesses, reaching values as low as −0.11 for the 1-ms data. This indicates that acquisition time rather than signal strength influences the offset despite the 15-nm film scattering three times more strongly than the 5-nm film.

Discussion

Negative Variance

Negative variance is physically meaningless and arises here because our correction procedure, equation (6), overcompensates for noise. A detailed derivation confirms that this equation is valid for a detector with DQE < 1, given discrete signals. To suppress runaway negative variance, it was proposed that the noise correction should be (Treacy et al., 2005):

$$\mathrm{nVarNC}(k_x, k_y) = \frac{\langle I^2(k_x, k_y)\rangle_N}{\langle I(k_x, k_y)\rangle_N^2} - 1 - \frac{Q}{\langle I(k_x, k_y)\rangle_N}. \qquad (7)$$

This assumed N is large ($N \gtrsim 100$). $Q \leq 1$ was thought (incorrectly) to be the DQE. With Q as an adjustable parameter, this correction worked well for low noise data not subjected to

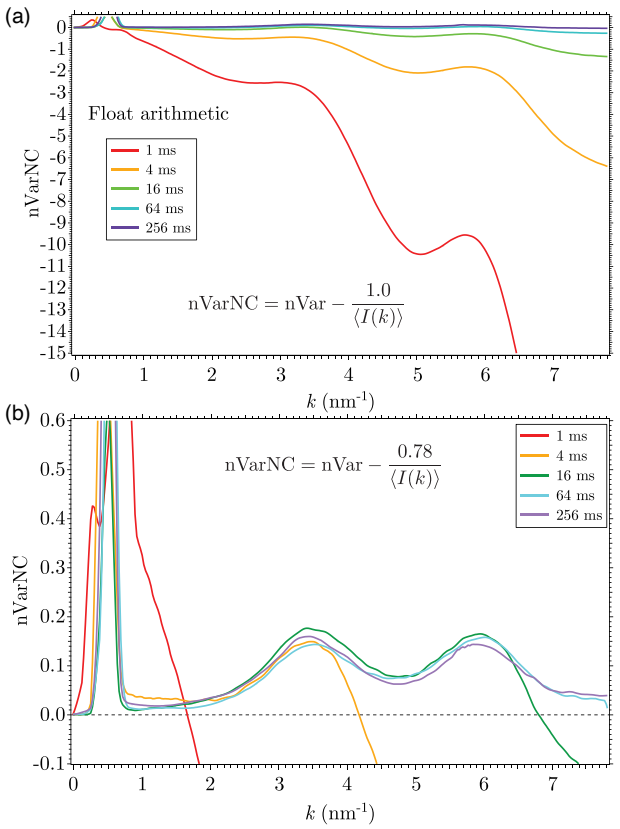

Fig. 8. Illustration of the difficulties encountered when removing Poisson noise from nondiscretized experimental radial variances obtained from 15-nm thickness amorphous Si. (**a**) Use of equation (6) overcorrects, and nVarNC becomes increasingly large and negative as k increases. (**b**) Use of equation (7) with $Q = 0.78$. The correction works best for the 256 ms data with the lowest noise. As acquisition time decreases, the threshold k value where the correction fails decreases.

`nint` thresholding. When intensity data are not discretized, the correct $Q = 1$ form leads to overcorrection, as shown in Figure 8a.

Negative variance is correctable using $Q = 0.78$, found by trial-and-error (Fig. 8b). This is significantly lower than the EMPAD DQE values of 0.88–0.93 reported by Tate et al. (2016). While this correction works for less noisy data collected at 256 ms, there is a critical k value above which nVarNC becomes negative and diverges, which decreases as acquisition time shortens. The noisiest 1-ms data are uncorrectable by (7) with $Q = 0.78$. However, the noise correction is stable with $Q = 1$ for `nint`-discretized data, demonstrated in Figure 7.

To explore this, we conducted FEM simulations on the 4,096-atom CRN model. The kinematical scattering simulations start as "noise-free" and emulate Poisson noise by assigning the number of electrons per diffraction pattern, integer M, to be proportional to the exposure time τ (Gibson & Treacy, 2008). The number of patterns, N, is adjusted to keep $N \times M = 10^7$, compliant with the constant-total-signal constraint of equation (3).

Figure 9a presents nVar simulations without noise correction for $M = 2{,}000$, 5,000, and 10,000 electrons per diffraction pattern, assuming a perfect detector. Most electrons concentrate in the central beam without signal dispersal (MTF = 1), eliminating the need for `nint`-thresholding. As in our experiments, shot noise dominates nVar, increasing with the scattering vector, while the noise-free simulation aligns with the expected nVar ≈ 1.0 for a CRN, as shown by the dark line compressed at the bottom of the plot.

In Figure 9b, the noise-corrected variance (nVarNC) is presented after subtracting $1/\langle I\rangle$ for discrete Poisson noise (Equation (6)). The black trace represents the "no noise" simulation. NVarNC hovers around 1.0 for weak signals, becoming noisier for $k > 10\,\mathrm{nm}^{-1}$. Although it may dip into negative values as mean intensity approaches zero, it generally varies around 1.0, confirming the correction's effectiveness. Notice the reduced noise in the intervals $2.5 \le k \le 3.5\,\mathrm{nm}^{-1}$ and $5.0 \le k \le 5.5\,\mathrm{nm}^{-1}$, where diffraction peaks from SRO in a-Si emerge.

We modified the computations to reflect the EMPAD's intensity-spread behavior. In the first model, we assumed up to 25% of the incident energy disperses over neighboring pixels, aligning with our observations of single-electron events on the EMPAD at 80 kV. Figure 9c shows that equation (6) ($Q = 1$) overcompensates for noise without `nint` thresholding, as observed in our raw data (compare Fig. 8a). We find by trial-and-error that $Q \approx 0.81$ corrects the expected nVarNC value to ≈ 1.0 (red plot). Unlike our data (Fig. 8b), the correction works well out to $k \approx 13\,\mathrm{nm}^{-1}$. Applying `nint`-thresholding fully restores the discrete signal because less than half of the pixel signal is lost (black noise-free plot in Fig. 9c), and Figure 9b is recovered with $Q = 1$. We note that the blue trace in Figure 9c shows peaks in the variance despite no MRO in the model. This is an artifact arising from the noise overcorrection.

This model emulates the average response characteristics of the EMPAD but does not capture all features shown in Figure 7. While the EMPAD retains about 75–80% of the signal on each pixel on average, some pixels lose over 50%.

In a second model, 100% of the incoming electron signal can disperse randomly over neighboring pixels. About half of the incident pixels, with less than 50% of the signal, will register 0, the other half registering 1. This dispersion decreases the mean intensity, $\langle I\rangle$, at each pixel and increases the normalized noise term, $1/\langle I\rangle$, leading to overcorrection.

Figure 9d shows nVarNC with `nint` thresholding and $Q = 1$. The black trace represents the simulation with no noise and a perfect detector. This second model reveals new features: (i) nVarNC suppression; (ii) nVarNC decreasing to negative values, particularly in the noisiest (red) curve; and (iii) emergence of broad low-noise peaks near 2.5–3.7 nm^{-1} and 4.2–6.2 nm^{-1}, consistent with experimental peaks in amorphous silicon. These peaks are absent in the idealized normalized variance plot (black trace) because the CRN model lacks MRO. A related finding by Rezikyan et al. (2015) noted variance suppression and the emergence of short-range order peaks when large random displacements of atoms were introduced. This model does not accurately reflect the EMPAD response, where most pixels retain over 50% of the incident electrons, meaning the large variance suppression in experiments is not fully explained.

It is worth emphasizing that the ratio $\langle I^2\rangle/\langle I\rangle^2$ in (7), which contains both signal and noise, should also be computed with `nint`-thresholding for the formula to work correctly.

The experimental nVarNC peaks are most pronounced in thicker films (Fig. 7). Yi & Voyles (2011) found that, with strong signal-to-noise, nVar scales inversely with specimen thickness. Treacy & Gibson (2012) showed that the background-subtracted peaks in the nVarNC scale as:

$$\left(\mathrm{nVarNC} - \frac{1}{m}\right)t = \text{constant}. \tag{8}$$

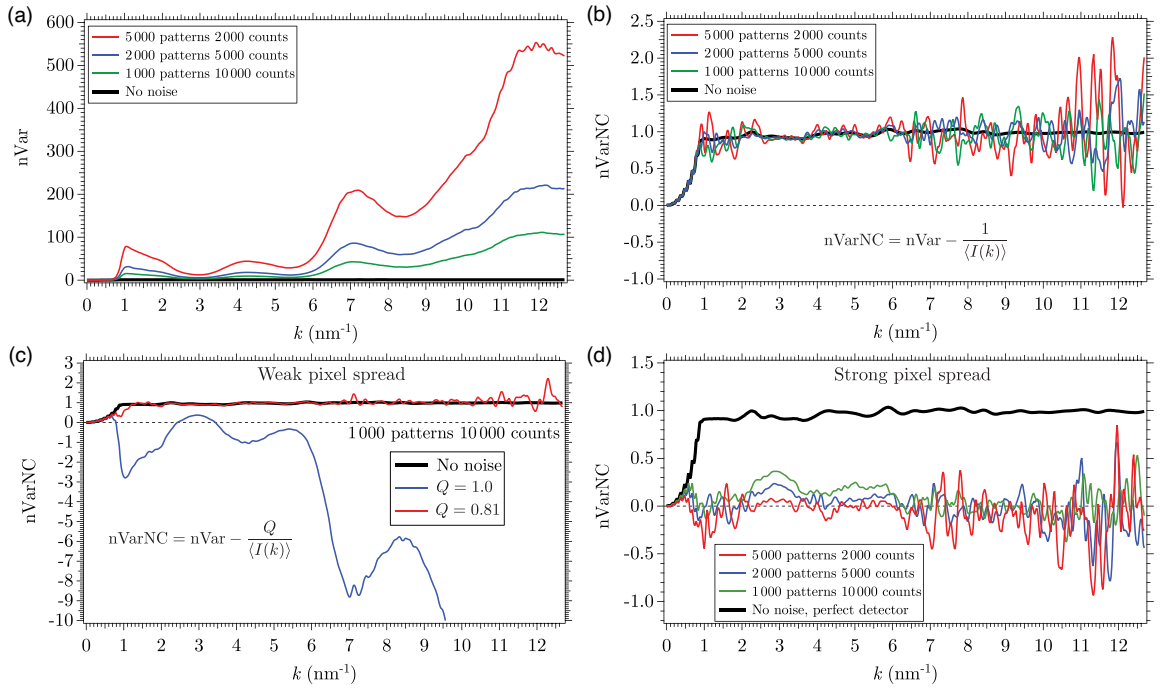

Fig. 9. Kinematical simulations of the radial normalized variance, nVar(k), from a 4,096-atom model of a continuous random network of amorphous Si. The total scattered electron count per simulation is held constant at $N \times M = 10^7$; 5,000 patterns with 2,000 counts total; 2,000 patterns with 5,000 counts total; and 1,000 patterns with 10,000 counts total. A high signal-to-noise ("No noise") simulation is also shown. (**a**) Normalized variances, computed according to equation (4) (with no `nint` thresholding). (**b**) Poisson-noise-corrected normalized variances, computed according to equation (6). (**c**) Noise-corrected normalized variances (with no `nint` thresholding) computed for the $N = 1{,}000$ patterns with $M = 10{,}000$ counts total, simulated with a nonideal detector that spreads some of the incoming signal intensity over neighboring pixels, similar to the EMPAD behavior. The blue line shows that equation (4) (for $Q = 1.0$) overcorrects the noise and that a lower value, $Q = 0.81$, removes the shot noise well (red curve). (**d**) Up to 100% of the electron signal is randomly dispersed among immediate-neighbor pixels. Here, we use `nint` thresholding with $Q = 1$. The variance drops to a value close to zero, with two broad peaks appearing in the windows $2.5 \leq k \leq 3.7\,\text{nm}^{-1}$ and $4.2 \leq k \leq 6.2\,\text{nm}^{-1}$, corresponding to the two principal experimental variance peaks for amorphous Si.

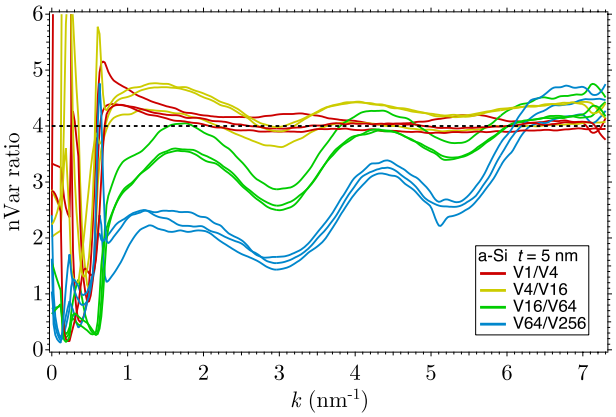

Fig. 10. Ratios of the experimental radial variances, nVar, for the 5-nm thickness Si. V1/V4 is the ratio of the 1 ms to the 4 ms nVar data, etc. The ratio of the noisiest data sets, V1/V4 (red), is dominated by Poisson noise and settles on the expected value of 4. The longer exposure times are less dominated by noise, and the variance from sample structural features starts to dominate.

As before, m is the illumination partial coherence parameter ($m \geq 1$). Since m tends to be large, the $1/m$ term is small and can be ignored, consistent with the findings of Yi & Voyles (2011). However, our data for different thicknesses (Fig. 7) do not conform to this expression, as nVarNC peak-to-dip profiles strengthen with increased thickness, contrary to equation (8). Possible explanations for this discrepancy include: (i) partial illumination coherence was different for each thickness; (ii) the decoherence contribution to m has a thickness dependence; (iii) the thinnest films are affected most by the oxide layers; or (iv) there are changes in the MRO characteristics in the thinnest films. We suspect differences in composition (iii) play a role in this discrepancy, although (iv) is an intriguing possibility.

Noise Randomness

Our analysis assumes stochastic noise—Poisson-distributed in the incident signal and random in the detector. This assumption can be tested. Since exposure times are decreased successively by factors of four in our experimental protocol, we expect the Poisson noise contribution to the normalized variance, $1/\langle I \rangle$, to increase successively by factors of four. To explore this, we examined the ratios of the non-noise-corrected variances, nVar, focusing on data sets differing by factors of four in acquisition time. Thus, we computed the ratios V1/V4 ≡ nVar(1 ms)/nVar(4 ms); V4/V16 ≡ nVar(4 ms)/nVar(16 ms), etc. The four resulting ratio plots are presented in Figure 10 for the 5-nm thickness amorphous Si. Data from three experimental runs at each exposure time confirm the reproducibility. The ratio V1/V4 (red curve) quickly settles to ~ 4.0 for $k \geq 2\,\text{nm}^{-1}$. This confirms that the dominant detector noise is also essentially random. The ratios in the less noisy data, V16/V64 and V64/V256, develop peaks with dips near $k = 3.1$ and $5.5\,\text{nm}^{-1}$. These arise because of the nonrandom variance contribution from the a-Si structure, which strengthens relative to the Poisson noise at the longer acquisition times.

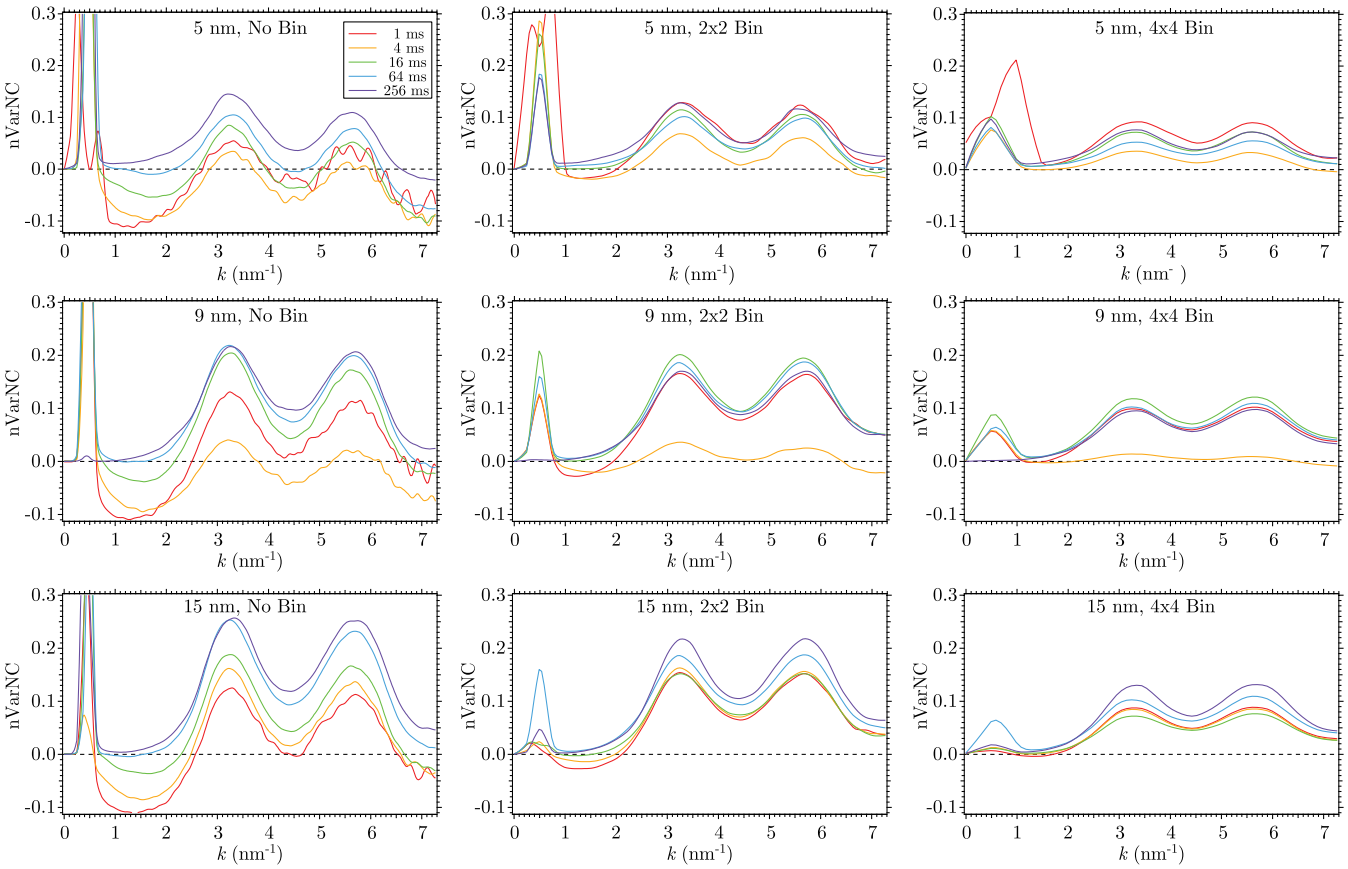

Fig. 11. Montage showing the noise-corrected radial variance data, nVarNC, after binning and `nint` thresholding. The rows are for the three thicknesses of amorphous silicon: 5, 9, and 15 nm. The columns are for different levels of binning. Left, no binning (similar to the data in Fig. 10, right column). Middle, binning 2 × 2 pixels; right, binning 4 × 4 pixels.

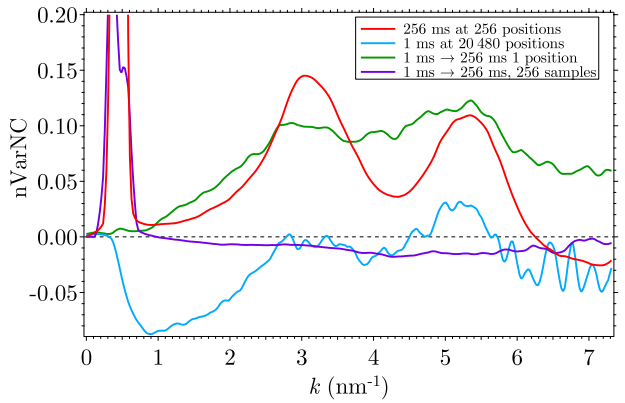

Fig. 12. Comparison of nVarNC for 5-nm thickness amorphous Si, using different experimental protocols. Red is for 256 diffraction patterns with 256 ms acquisition time. Blue is the variance of 20,480 1-ms separate diffraction patterns, all taken from the same nominal sample location. Green takes the same 20,480-pattern dataset, merging 256 successive patterns at a time to form eighty 256-ms-equivalent patterns. Purple takes 65,536 1-ms patterns from different sample volumes, accumulating 256 successive patterns at a time to create the equivalent of 256 × 256-ms patterns. This mimics strong decoherence.

Binning

Binning pixel data is known to improve the signal-to-noise in the enlarged camera pixels. Radić et al. (2022) demonstrated that on-chip binning has advantages over postprocessing in their FEM study. For the EMPAD camera's 128 × 128 pixel array, binning can significantly reduce resolution along k. Figure 11 shows the results of 2 × 2 and 4 × 4 postprocessing binning of our EMPAD data across the three amorphous Si thicknesses. The first column presents unbinned nVarNC plots from Figure 7 for comparison; the center column shows 2 × 2 binning, and the right column shows 4 × 4 binning. The variance peaks lose definition with binning, especially with 4 × 4. The negative variance offset decreases by about a factor of 4 for 2 × 2 and roughly 16 for 4 × 4. Overall, resolution along k is significantly degraded, with only 16 effective data pixels remaining.

The Reciprocity Theorem indicates that binning mutually incoherent detector pixels in k space effectively decreases spatial coherence for a coherent point source. This is observed as a reduction in the height of variance peaks with 4 × 4 binning. A larger binned pixel represents an increasingly incoherent source (larger m), subtending a greater solid angle at the sample. The coherence width at the sample scales as $\sim 1/\Delta k$, where Δk is the width of the binned pixels in reciprocal space.

Our diffraction data have a central disk diameter of about nine pixels, indicating it was oversampled, which reduces the detector-based contribution to incoherence. The 2 × 2 binned data remains oversampled with minimal impact on nVarNC peak heights, while 4 × 4 binning shows a noticeable drop in these peaks from hitting the sampling limit. The 2 × 2 binning improves variance without significantly affecting coherence. In addition to enhancing signal-to-noise, binning helps compensate for signal spreading by increasing the equivalent pixel size.

Serial Diffraction

This study posited that a diffraction pattern collected over 256 ms is equivalent to the sum of 256 consecutive 1-ms patterns. We hypothesized that such a temporal breakdown of the data could identify the slower contributions to FEM decoherence, but our FEM variance data showed no improvement. Our ECM data from fixed sample regions allow us to monitor temporal changes. Since the EMPAD readout time is 0.86 ms, a 256-ms pattern takes 476 ms to accumulate from 256 consecutive 1-ms patterns, so the elapsed times do not match.

Figure 12 compares four serial accumulations of the nVarNC data. The red curve is the 256-ms normalized variance from Figure 7 (top-right). The blue curve, derived from 20,480 1-ms diffraction patterns from the same region acquired over 38.1 s, is noisier but exhibits a negative offset similar to that in Figure 7. The presence of variance peaks indicates that subtle structural changes occurred during acquisition.

The green curve, derived from the same dataset, merges successive blocks of 256 patterns to construct 80 patterns, each with a 256 ms signal time but requiring 476 ms to accumulate. The green curve should show low variance if the summed patterns are similar, but instead, it shows significant variance, albeit with less defined peaks. The ECM plot from Figure 5 suggests correlation times are around 272 ms, predicting measurable differences in the summed patterns. The pronounced peaks from the red curve are observed but with reduced definition. Readout and dark noise from the EMPAD do not significantly affect the normalized variance, as changing the number of diffraction patterns in the analysis does not impact the offset.

The purple curve represents the outcome of processing 65,536 1-ms patterns from different sample areas, producing 256×256-ms summed patterns. Since consecutive patterns come from different regions, this mimics severe displacement decoherence. The variance nVarNC is near zero with no identifiable peaks, although there is a slight negative variance beyond the central disk. Treating this residual variance as a measure of the nonstochastic contributions is tempting. However, it does not correct the negative variance of the red curve past $k > 6.2\,\mathrm{nm}^{-1}$. We note that thickness variations across the probed areas would produce a positive residual variance.

Conclusions

This study explored the hypothesis that rapid acquisition of STFEM diffraction data could reduce decoherence effects, enhancing both peak and background FEM variance. We found no significant enhancement in the noise-corrected normalized variance *peaks* from MRO in amorphous Si with acquisition times faster than about 1/4 s.

Data from ECM supports this, showing a correlation decay time of around 1/4 s in a-Si diffraction patterns. Although we note a minor improvement in variance down to 64 ms acquisition times, the increased difficulty of noise removal outweighs the benefit.

The observed decay time is slower than anticipated, as previous studies suggested that decoherence processes might occur at shorter time scales. Our experiment focused on structural changes slower than 1 ms. Thus, higher-frequency decoherence events remain an unconfirmed possibility.

We still do not know why background variance in FEM is so strongly suppressed. It remains unclear what the beam-sample changes are, likely sample-dependent, over timescales shorter than 1 ms. Simulations confirm that phonons are not primarily responsible (Rezikyan et al., 2015). Sample-charge fluctuations (currents) may play a more significant role in STFEM than previously suspected (Russo & Henderson, 2018). All electrons in the focused beam pass close to the varying charge building up in the irradiated region, possibly with accumulating damage (Jiang, 2016). Incoherence is associated with the concentrated illumination source, whereas decoherence is thought to be associated with the concentrated beam crossover at the specimen—at least in STFEM. A comparison of STFEM and TDFEM variance data would be instructive, as the illumination fluence rates at the specimen differ by orders of magnitude. Rapid-acquisition TDFEM, being image-based, may facilitate specimen-drift correction.

Noise correction dominated our analysis. Employing a nearest-integer-electron threshold to pixel intensity restored much of the Poisson noise characteristics. As acquisition time decreased, a residual overcorrection in nVarNC appeared, apparently not significantly tied to detector readout noise, which impeded analysis of the absolute variance *background* values. Pixel binning improves the signal-to-noise ratio and lessens the impact of signal spreading with a possible loss of spatial coherence.

A fast electron detector with precise pulse counting is highly desirable for Poisson noise correction in low fluence FEM studies.

Availability of Data and Materials

The authors have declared that no datasets apply for this piece.

Acknowledgments

M.M.J.T. thanks Ruud Tromp (IBM) and Penghan Lu (Jülich) for valuable discussions.

Author Contributions Statement

A.Z. helped devise experimental protocols, collected and analyzed data, and contributed codes for the analysis. H.D. helped devise experimental protocols and conducted TEM experiments. R.E.D.-B. helped devise experiments and contributed to the analysis. J.M.G. conducted TEM experiments and contributed to the analysis. A.R. contributed to the experiment design, provided samples, and conducted TEM experiments. M.M.J.T. devised and supervised the experiments, contributed codes for analysis, and wrote the first draft. All authors contributed to the manuscript write-up.

Financial Support

National Science Foundation (NSF Award Number 1906367) and by the Ernst Ruska-Centre for Microscopy and Spectroscopy with Electrons, Jülich.

Conflict of Interest

No competing interest is declared.

References

Borisenko KB, Haberl B, Liu ACY, Chen Y, Li G, Williams JS, Bradby JE, Cockayne DJH & Treacy MMJ (2012). Medium-range order in amorphous silicon investigated by constrained structural relaxation of two-body and four-body electron diffraction data. *Acta Mater* **60**(1), 359–375. https://doi.org/10.1016/j.actamat.2011.09.039

Born M & Wolf E (2013). *Principles of Optics: Electromagnetic Theory of Propagation, Interference and Diffraction of Light*. Oxford: Elsevier.

Cockayne DJH (2007). The study of nanovolumes of amorphous materials using electron scattering. *Annu Rev Mater Res* **37**(1), 159–187. https://doi.org/10.1146/matsci.2007.37.issue-1

Cockayne DJH & McKenzie DR (1988). Electron diffraction analysis of polycrystalline and amorphous thin films. *Acta Crystallogr A* **44**(6), 870–878. https://doi.org/10.1107/S0108767388004957

Dainty JC (1975). Stellar speckle interferometry. In *Laser Speckle and Related Phenomena*, Dainty JC (Ed.), pp. 255–280. New York: Springer-Verlag.

Daulton TL, Bondi KS & Kelton KF (2010). Nanobeam diffraction fluctuation electron microscopy technique for structural characterization of disordered materials–application to AL88-xY7Fe5Tix metallic glasses. *Ultramicroscopy* **110**(10), 1279–1289. http://www.sciencedirect.com/science/article/pii/S030439911000166X. https://doi.org/10.1016/j.ultramic.2010.05.010

Gibson JM & Howie A (1979). Investigation of local structure and composition in amorphous solids by high resolution electron microscopy. In *Special Issue, Nobel Symposium 47, "Direct Imaging of Atoms in Crystals and Molecules," Lidingo, Sweden, Aug. 1979*, vol. 14, pp. 109–116. Cambridge.

Gibson JM & Treacy MMJ (2008). Beam transit effects in single molecule coherent diffraction. *Phys Rev B Condens Matter Mater Phys* **78**(24), 245401. https://doi.org/10.1103/PhysRevB.78.245401

Goodman J (1975*a*). Probability density function of the sum of n partially correlated speckle patterns. *Opt Commun* **13**(3), 244–247. https://doi.org/10.1016/0030-4018(75)90091-7

Goodman JW (1975*b*). Some fundamental properties of speckle. In *Laser Speckle and Related Phenomena*, Dainty JC (Ed.), pp. 60–68. New York: Springer-Verlag.

Huang S & Voyles PM (2024). Momentum transfer resolved electron correlation microscopy. *Ultramicroscopy* **256**, 113886. https://doi.org/10.1016/j.ultramic.2023.113886

Jiang N (2015). Electron beam damage in oxides: A review. *Rep Prog Phys* **79**(1), 016501. https://doi.org/10.1088/0034-4885/79/1/016501

Jiang N (2016). Beam damage by the induced electric field in transmission electron microscopy. *Micron* **83**, 79–92. https://doi.org/10.1016/j.micron.2016.02.007

Jiang N (2023). Electron irradiation effects in transmission electron microscopy: Random displacements and collective migrations. *Micron* **171**(1), 103482. https://doi.org/10.1016/j.micron.2023.103482

Kalay Y, Kalay I, Hwang J, Voyles P & Kramer M (2012). Local chemical and topological order in AL–TB and its role in controlling nanocrystal formation. *Acta Mater* **60**(3), 994–1003. https://doi.org/10.1016/j.actamat.2011.11.008

Kodama T, Nakashima Y, Akashi T, Takahashi Y, Mori S & Harada K (2022). Analysis of spatial point patterns in electron-counting images. *Microscopy* **71**(3), 142–151. https://doi.org/10.1093/jmicro/dfac006

Lee Z, Rose H, Lehtinen O, Biskupek J & Kaiser U (2014). Electron dose dependence of signal-to-noise ratio, atom contrast and resolution in transmission electron microscope images. *Ultramicroscopy* **145**(1), 3–12. https://doi.org/10.1016/j.ultramic.2014.01.010

Levin BDA (2021). Direct detectors and their applications in electron microscopy for materials science. *JPhys Mater* **4**, 042005. https://doi.org/10.1088/2515-7639/ac0ff9

Maldonis JJ, Hwang J & Voyles PM (2017). FEMSIM + HRMC: Simulation of and structural refinement using fluctuation electron microscopy for amorphous materials. *Comput Phys Commun* **213**, 217–222. https://doi.org/10.1016/j.cpc.2016.12.006

Nellist PD, McCallum BC & Rodenburg JM (1995). Resolution beyond the "information limit" in transmission electron microscopy. *Nature* **374**(6523), 630–632. https://doi.org/10.1038/374630a0

Ophus C (2019). Four-dimensional scanning transmission electron microscopy (4D-stem): From scanning nanodiffraction to ptychography and beyond. *Microsc Microanal* **25**(3), 563–582. https://doi.org/10.1017/S1431927619000497

Press WH, Teukolsky SA, Vetterling WT & Flannery BP (1992). *Numerical Recipes in C: The Art of Scientific Computing*, 2nd ed. Cambridge: Cambridge University Press.

Radić D, Hilke S, Peterlechner M, Posselt M & Bracht H (2019). Fluctuation electron microscopy on silicon amorphized at varying self ion-implantation conditions. *J Appl Phys* **126**(9), 095707. https://doi.org/10.1063/1.5107494

Radić D, Peterlechner M, Posselt M & Bracht H (2022). Treating knock-on displacements in fluctuation electron microscopy experiments. *Microsc Microanal* **28**(6), 2036–2046. https://doi.org/10.1017/S1431927622012417

Rezikyan A, Jibben ZJ, Rock BA, Zhao G, Koeck FAM, Nemanich RF & Treacy MMJ (2015). Speckle suppression by decoherence in fluctuation electron microscopy. *Microsc Microanal* **21**(6), 1455–1474. https://doi.org/10.1017/S1431927615015135

Ruskin AI, Yu Z & Grigorieff N (2013). Quantitative characterization of electron detectors for transmission electron microscopy. *J Struct Biol* **184**(3), 385–393. https://doi.org/10.1016/j.jsb.2013.10.016

Russo CJ & Henderson R (2018). Charge accumulation in electron cryomicroscopy. *Ultramicroscopy* **187**(02), 43–49. https://doi.org/10.1016/j.ultramic.2018.01.009

Schneider CA, Rasband WS & Eliceiri KW (2012). NIH image to imageJ: 25 years of image analysis. *Nat Methods* **9**(7), 671–675. https://doi.org/10.1038/nmeth.2089

Tate MW, Purohit P, Chamberlain D, Nguyen KX, Hovden R, Chang CS, Deb P, Turgut E, Heron JT, Schlom DG, Ralph DC, Fuchs GD, Shanks KS, Philipp HT, Muller DA & Gruner SM (2016). High dynamic range pixel array detector for scanning transmission electron microscopy. *Microsc Microanal* **22**(1), 237–249. https://doi.org/10.1017/S1431927615015664

Treacy MMJ (2012). Speckles in images and diffraction patterns. In chapter 12. pp. 405–435. Cambridge: John Wiley & Sons, Ltd. https://doi.org/10.1002/9783527641864.ch12

Treacy MMJ & Borisenko KB (2012). The local structure of amorphous silicon. *Science* **335**(6071), 950–953. Experimentally, a-Si typically has a density about 1 to 2% less than that of the cubic crystalline phase. https://doi.org/10.1126/science.1214780

Treacy MMJ & Gibson JM (1996). Variable coherence microscopy: A rich source of structural information from disordered materials. *Acta Crystallogr A* **52**(2), 212–220. https://doi.org/10.1107/S0108767395012876

Treacy MMJ & Gibson JM (1998). Statistics of partially coherent dark-field images of amorphous materials. *In Electron Microscopy and Analysis 1997, Inst Phys Conf Ser No 153, (Institute of Physics, London)*, Rodenburg JM (Ed.), pp. 433–436. Boca Raton: CRC Press.

Treacy MMJ & Gibson JM (2012). Examination of a polycrystalline thin-film model to explore the relation between probe size and structural correlation length in fluctuation electron microscopy. *Microsc Microanal* **18**(1), 241–253. https://doi.org/10.1017/S1431927611012517

Treacy MMJ, Gibson JM, Fan L, Paterson DJ & McNulty I (2005). Fluctuation microscopy: A probe of medium range order. *Rep Prog Phys* **68**(12), 2899–2944. https://doi.org/10.1088/0034-4885/68/12/R06

Treacy MMJ, Gibson JM & Keblinski PJ (1998). Paracrystallites found in evaporated amorphous tetrahedral semiconductors. *J Non Cryst Solids* **231**(1-2), 99–110. https://doi.org/10.1016/S0022-3093(98)00371-8

Vaerst O, Wilde G & Peterlechner M (2023). Beam effects on atomic dynamics in metallic glasses studied with electron correlation microscopy. *Microsc Microanal* **29**(6), 1870–1878. https://doi.org/10.1093/micmic/ozad110

Wooten F, Winer K & Weaire D (1985). Computer generation of structural models of amorphous Si and Ge. *Phys Rev Lett* **54**(13), 1392–1395. https://doi.org/10.1103/PhysRevLett.54.1392

Yi F & Voyles PM (2011). Effect of sample thickness, energy filtering, and probe coherence on fluctuation electron microscopy experiments. *Ultramicroscopy* **111**(8), 1375–1380. https://doi.org/10.1016/j.ultramic.2011.05.004

Zjajo A, Matzkevich I, Rezikyan A, Du H & Dunin-Borkowski RE (2021). Estimating illumination coherence width from focused-probe intensity profiles. *Microsc Microanal* **27**(S1), 738–740. https://doi.org/10.1017/S1431927621002981

Appendix: An analytical model of non-Poisson noise

As Figure 4 shows, many electron-detection events spread energy over neighboring pixels. The low-intensity histogram in Figure 3 shows a significant intensity spread between the discrete-valued peaks. We presented a computational model showing how this affects the normalized variance from a model CRN (Fig. 8). However, an analytical mathematical model of the impact on Poisson noise variance is useful.

We treat the incident signal as Poisson distributed, with events arriving with a probability distribution given by equation (5). If there are q arriving events at a pixel, this becomes dispersed as an intensity I in the histogram by a dispersal function $G(I, q)$. Thus, the intensity I is given by the probability distribution

$$P(I) = \sum_{q=0}^{\infty} G(I, q) \frac{\langle q \rangle^q}{q!} \mathrm{e}^{-\langle q \rangle}. \tag{A.1}$$

This transforms the red delta-function peaks in Figure 3 into a continuous distribution, such as the black curve. The mean intensity is then

$$\langle I \rangle = \sum_{q=0}^{\infty} \frac{\langle q \rangle^q}{q!} \mathrm{e}^{-\langle q \rangle} \int_0^{\infty} I G(I, q)\, \mathrm{d}I, \tag{A.2}$$

and the second moment is

$$\langle I^2 \rangle = \sum_{q=0}^{\infty} \frac{\langle q \rangle^q}{q!} \mathrm{e}^{-\langle q \rangle} \int_0^{\infty} I^2 G(I, q)\, \mathrm{d}I. \tag{A.3}$$

We assume the dispersal function $G(I, q)$ conserves total energy (signal). The second moment of intensity, and thereby the normalized variance (equation (4)), is expected to increase because we now include the continuum of smaller noninteger values I in the statistics and do not restrict the values of I to the discrete q. If the detector were perfect, we would replace $G(I, q)$ with a Dirac delta function, $G(I, q) \doteq \delta(I - q)$, restoring $\mathrm{nVar} = 1/\langle q \rangle$ for the Poisson noise.

For analytical simplicity, we model the $G(I, q)$ as Gaussians,

$$G(I, q) = \frac{1}{\sqrt{2\pi}\sigma_q} \exp\left(-\frac{(I - q)^2}{2\sigma_q^2} \right). \tag{A.4}$$

Strictly, the $G(I, q)$ functions must maintain a positive signal $I \geq 0$: the signal dispersal should not create a negative intensity anywhere. The model is acceptable if σ_q is kept small. Gaussians do not precisely reproduce the intensity histograms (Fig. 3), but the essential feature (intensity between discrete peaks) is reproduced.

Since the signal from q electrons, assumed to be arriving separately, is the $(q - 1)$-fold convolution of the response function for a single electron arrival, we write the variances as

$$\sigma_q^2 = \begin{cases} \sigma_0^2 & q = 0, \\ q(\sigma_0^2 + \sigma_\mathrm{d}^2) & q > 0. \end{cases} \tag{A.5}$$

σ_0 is the standard deviation of the detector noise on the zero peak, and σ_d is the standard deviation of the signal generated within the detector by the arrival of one electron. This has to be added to the variance of the zero level, σ_0^2, which is present at each electron arrival event.

With Gaussians, the integrals in Equations (A.2) and (A.3) give

$$\langle I \rangle = \sum_{q=0}^{\infty} \frac{\langle q \rangle^q}{q!} \mathrm{e}^{-\langle q \rangle} \left[\frac{\sigma_q}{\sqrt{2\pi}} \exp\left(-q^2 / 2\sigma_q^2 \right) + \frac{1}{2}\left(q^2 + \sigma_q^2 \right)\left(1 - \mathrm{erf}\left(-q/\sqrt{2}\sigma_q \right) \right) \right], \tag{A.6}$$

and

$$\langle I^2 \rangle = \sum_{q=0}^{\infty} \frac{\langle q \rangle^q}{q!} \mathrm{e}^{-\langle q \rangle} \left[\frac{3q\sigma_q}{\sqrt{2\pi}} \exp\left(-q^2 / 2\sigma_q^2 \right) + \frac{q}{2}\left(1 - \mathrm{erf}\left(-q/\sqrt{2}\sigma_q \right) \right) \right], \tag{A.7}$$

from which we obtain nVar using equation (4).

Figure A.1 shows simulations using this model, setting $\sigma_0 = 0$; and $\sigma_\mathrm{d} = 0.0$ (Poisson), 0.5, and 1.0 respectively. This confirms that the normalized noise variance is *increased* by the signal spread ($\sigma_q > 0$) relative to that expected from Poisson noise.

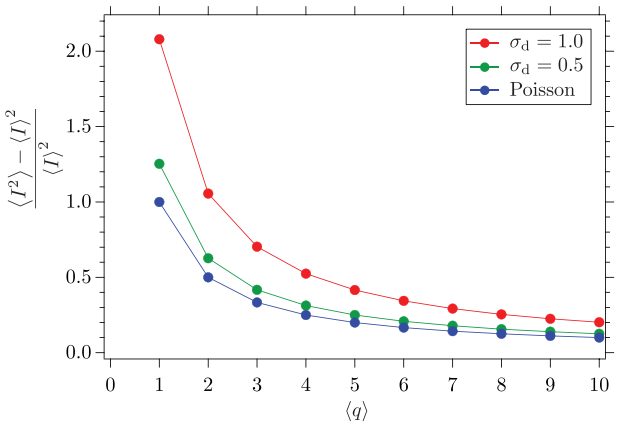

Fig. A.1. Results of an analytical model showing how pixel spread affects the normalized variance of detected shot noise. Blue shows nVar for the idealized Poisson model. The green and red curves are based on signal spread models where the detector does not have a delta function response to incoming electrons. This spread increases the normalized variance relative to the idealized Poisson value.